

Demonstration of a Broadband Photodetector Based on a Two-Dimensional Metal–Organic Framework

Himani Arora,* Renhao Dong, Tommaso Venanzi, Jens Zscharschuch, Harald Schneider, Manfred Helm, Xinliang Feng, Enrique Cánovas,* and Artur Erbe*

Metal–organic frameworks (MOFs) are emerging as an appealing class of highly tailorable electrically conducting materials with potential applications in optoelectronics. Yet, the realization of their proof-of-concept devices remains a daunting challenge, attributed to their poor electrical properties. Following recent work on a semiconducting $\text{Fe}_3(\text{THT})_2(\text{NH}_4)_3$ (THT: 2,3,6,7,10,11-triphenylenehexathiol) 2D MOF with record-high mobility and band-like charge transport, here, an $\text{Fe}_3(\text{THT})_2(\text{NH}_4)_3$ MOF-based photodetector operating in photoconductive mode capable of detecting a broad wavelength range from UV to NIR (400–1575 nm) is demonstrated. The narrow IR bandgap of the active layer (≈ 0.45 eV) constrains the performance of the photodetector at room temperature by band-to-band thermal excitation of charge carriers. At 77 K, the device performance is significantly improved; two orders of magnitude higher voltage responsivity, lower noise equivalent power, and higher specific detectivity of $7 \times 10^8 \text{ cm Hz}^{1/2} \text{ W}^{-1}$ are achieved under 785 nm excitation. These figures of merit are retained over the analyzed spectral region (400–1575 nm) and are commensurate to those obtained with the first demonstrations of graphene- and black-phosphorus-based photodetectors. This work demonstrates the feasibility of integrating conjugated MOFs as an active element into broadband photodetectors, thus bridging the gap between materials' synthesis and technological applications.

Though the majority of MOFs are known to be electrical insulators, advances in synthetic approaches over the past decade have revealed several examples of (semi)conductive MOFs,^[13–25] an aspect that allows their use in (opto)electronic applications as an active element. While some works demonstrate their semiconducting behavior,^[15–18] others have revealed them behaving as either metals or semimetals,^[21,24–26] that is, lacking a bandgap. Among them, graphene-like MOF analogues, where 2D hexagonal lattices are obtained from trigonal organic ligands coordinated by square-planar atomic metal nodes, have emerged as a unique sub-class of electrically conducting materials. In general, these 2D MOF samples display a variety of electrical properties, which can be linked to intrinsic and/or extrinsic factors. In most cases, the samples are produced in powder form, and later pressed into pellets to characterize their conductive properties as a function of temperature. Broadly speaking, most works revealed thermally activated charge transport mechanisms and low charge carrier mobilities, which might be (to a large

extent) linked to the polycrystalline nature of the produced pellets. MOFs with such features are particularly unsuitable for device prototyping, where large-area MOF thin films displaying semiconducting properties (with a defined bandgap) and delocalized charge carrier transport are required. These ideal features for device development were recently reported by us on a novel semiconducting $\text{Fe}_3(\text{THT})_2(\text{NH}_4)_3$ (THT: 2,3,6,7,10,11-triphenylenehexathiol) 2D MOF produced by an interfacial synthesis


extent) linked to the polycrystalline nature of the produced pellets. MOFs with such features are particularly unsuitable for device prototyping, where large-area MOF thin films displaying semiconducting properties (with a defined bandgap) and delocalized charge carrier transport are required. These ideal features for device development were recently reported by us on a novel semiconducting $\text{Fe}_3(\text{THT})_2(\text{NH}_4)_3$ (THT: 2,3,6,7,10,11-triphenylenehexathiol) 2D MOF produced by an interfacial synthesis

H. Arora, T. Venanzi, J. Zscharschuch, Dr. H. Schneider, Prof. M. Helm, Dr. A. Erbe
Institute of Ion Beam Physics and Materials Research
Helmholtz-Zentrum Dresden-Rossendorf
Dresden 01328, Germany
E-mail: h.arora@hzdr.de; a.erbe@hzdr.de

H. Arora, T. Venanzi, Prof. M. Helm
Faculty of Physics and Center for Advancing Electronics Dresden
Technische Universität Dresden
Dresden 01062, Germany

Dr. R. Dong, Prof. X. Feng
Faculty of Chemistry and Food Chemistry and Center for Advancing Electronics Dresden
Technische Universität Dresden
Dresden 01062, Germany

Dr. E. Cánovas
Instituto Madrileño de Estudios Avanzados en Nanociencia (IMDEA Nanociencia)
Madrid 28049, Spain
E-mail: enrique.canovas@imdea.org

 The ORCID identification number(s) for the author(s) of this article can be found under <https://doi.org/10.1002/adma.201907063>.

© 2020 The Authors. Published by WILEY-VCH Verlag GmbH & Co. KGaA, Weinheim. This is an open access article under the terms of the Creative Commons Attribution License, which permits use, distribution and reproduction in any medium, provided the original work is properly cited.

DOI: 10.1002/adma.201907063

protocol (ref. [17]). A spontaneous reaction at the $\text{CHCl}_3/\text{water}$ interface allows the formation of large-area free-standing multilayered films with tunable thicknesses that can be readily controlled. More importantly, these samples are characterized by a direct bandgap in the IR region and a charge carrier mobility of $230 \text{ cm}^2 \text{ V}^{-1} \text{ s}^{-1}$ at room temperature (measured by Hall-effect over channel lengths of few hundreds micrometers). These appealing characteristics of the reported samples open the path to exploiting them as active elements in optoelectronic devices.

In this work, we demonstrate the ability of free-standing 2D MOF films of $\text{Fe}_3(\text{THT})_2(\text{NH}_4)_3$ to serve as an active element in a two-terminal photodetector device. Changes in device conductance are revealed upon light exposure ranging from UV to NIR wavelengths (400–1575 nm). Temperature-dependent photocurrent measurements demonstrate that the photodetector shows a stronger photoresponse and higher sensitivity at liquid nitrogen temperatures (77 K) than at room temperature. In addition, a drastic improvement in photodetector's figures of merit, such as photosensitivity (defined as the ratio of photocurrent to dark current), voltage responsivity (R_v), noise equivalent power (NEP) and specific detectivity (D^*), is achieved on cooling the devices to 77 K. These results are consistent with the low IR bandgap of the samples, which causes strong thermally activated band-to-band population of free charge carriers at room temperature, described by $N \propto \exp[-E_g/2kT]$. Cooling the devices suppresses this thermal generation of charge carriers, which consequently leads to much improved device performance. Furthermore, the devices show stable and reproducible photoswitching behavior as a function of time. To the best of our knowledge, such broadband photoresponse is being reported for the first time for an entirely 2D MOF-based photodetector and demonstrates a reliable and robust device.

The thin films of $\text{Fe}_3(\text{THT})_2(\text{NH}_4)_3$ are synthesized by a spontaneous reaction at the $\text{CHCl}_3/\text{water}$ interface hosting iron precursors and THT, respectively, under argon atmosphere at room temperature. Depending on the reaction time, the film thickness can be widely tailored, from 20 nm up to several μm . An in-depth characterization and analysis of the material's structure has confirmed the high-quality polycrystalline nature of as-prepared $\text{Fe}_3(\text{THT})_2(\text{NH}_4)_3$ MOF films as reported in our previous work (ref. [17]) (note that a detailed summary of the results obtained from characterization and analysis of the material's structure and electronic properties is provided in Supporting Information). Structurally, a monolayer of $\text{Fe}_3(\text{THT})_2(\text{NH}_4)_3$ MOF film (shown in Figure 1a) possesses a planar hexagonal geometry extended into two directions, thus, forming a 2D network. Within a monolayer, the Fe metal and THT organic ligands are bonded in a honeycomb structure with a pore size of $\approx 1.9 \text{ nm}$, as shown in Figure 1b. When these 2D monolayers superimpose via van der Waals interactions, flat and crack-free multilayered structures with typical lateral dimensions of few millimeters are formed. In this study, free-standing $1.7 \mu\text{m}$ thick MOF films are used to fabricate the photodetector devices. As revealed by the Tauc plot in Figure 1c, the samples are characterized by a direct bandgap with an absorption edge of $\approx 0.45 \text{ eV}$. A two-terminal device (schematic in Figure 1d) is fabricated from a MOF flake bonded to an insulating glass substrate by using high-quality indium metal electrodes (chemPUR, 99.99% purity). The optical micrographs of actual devices are shown in Figure S1, Supporting Information. The device consists of a $1.7 \mu\text{m}$ thick MOF layer with an active area $A \approx 0.7 \text{ mm}^2$, defined by channel length $L \approx 1 \text{ mm}$, and width $W \approx 0.7 \text{ mm}$.

The photoresponse of the developed MOF-based photodetector is initially characterized under 785 nm laser irradiation,

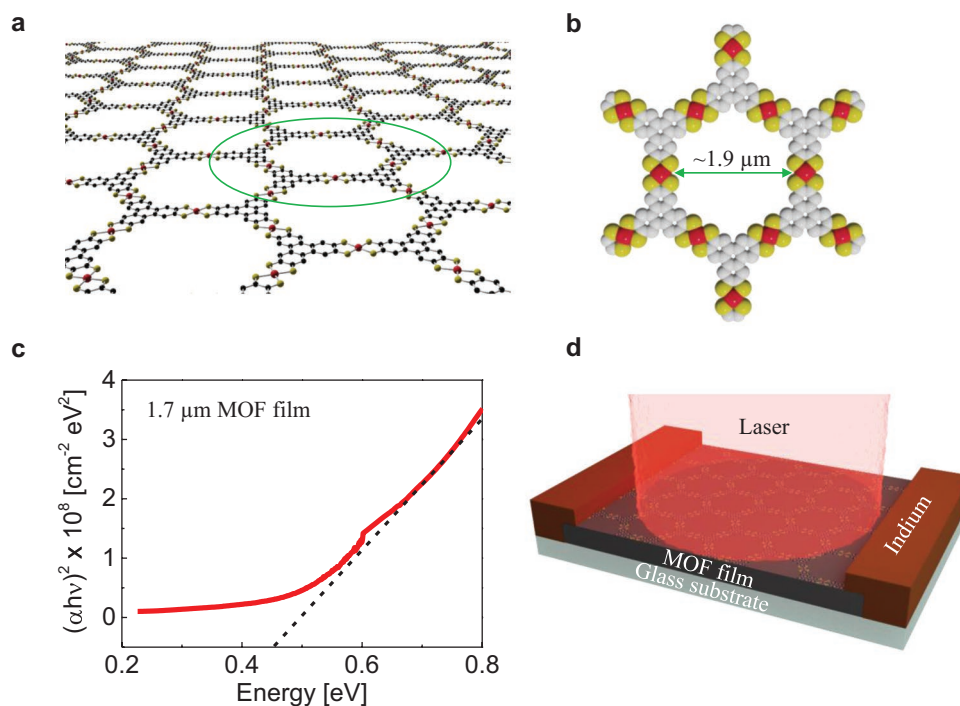


Figure 1. Material description and device fabrication. a) Schematic of a monolayer of $\text{Fe}_3(\text{THT})_2(\text{NH}_4)_3$ 2D MOF film investigated in this study. b) Chemical structure of the MOF film, Fe metal and THT organic ligands are bonded via sulfur in a honeycomb structure with a pore size of $\approx 1.9 \text{ nm}$. Color code: red spheres represent iron atoms, yellow refers to sulfur atoms, and gray represents benzene rings. c) Tauc plot for $1.7 \mu\text{m}$ thick MOF film at room temperature, revealing an optical bandgap of $\approx 0.45 \text{ eV}$. d) Schematic of a two-terminal photodetector device based on $1.7 \mu\text{m}$ thick MOF layer with indium electrodes.

and subsequently at 405, 633, and 1575 nm, at various power settings. The spot size of the laser is ≈ 2 mm in diameter, assuring full illumination of the device active area. All electrical characterizations, with and without illumination, are carried out in vacuum ($<10^{-7}$ mbar) by applying a sweeping bias of ± 1 V in the temperature range of 77–300 K. For the whole temperature range, all analyzed MOF-devices are found to yield hysteresis-free current–voltage (I – V) characteristics, both in dark condition and under illumination.

Figure 2a,b shows the I – V characteristics of the MOF-device as a function of incident laser power densities (P) at 785 nm at 300 and 77 K, respectively. Both curves reveal an increase in the photocurrent with increasing photon density, demonstrating the operation of the active MOF layer as a photoconductor at both temperatures. In order to precisely interrogate the effect of temperature on the performance of the photodetector, we measured the photoresponse of the sample in the temperature range of 77–300 K under various fluences of 785 nm illumination. Figure 2c shows current (at a bias of -1 V) as a function of

inverse temperature ($1/T$) measured in dark (black curve) and under different 785 nm light intensities ranging from 0.026 (red curve) to 0.60 (orange curve) W cm^{-2} (I – V curves measured in dark in the temperature range of 77–300 K are shown in Figure S2, Supporting Information). The obtained trend is consistent with the narrow IR bandgap of the samples, enabling thermally activated charge carrier population of the conduction and valence bands at higher temperatures (in agreement with our previous findings, where the 1.7 μm thick sample revealed a thermally activated carrier density population, described by $N \propto \exp[-E_g/2kT]$. From Hall measurements, a charge density of $6.2 \times 10^{14} \text{ cm}^{-3}$ was obtained at 300 K, which decreased to $2.0 \times 10^{11} \text{ cm}^{-3}$ at 100 K, ref. [17]). On fitting the exponential function, an activation energy of 0.35 ± 0.1 eV is extracted from I versus $1/T$ plot, which is comparable to the optical bandgap of 0.45 eV resolved for the samples. At higher temperatures ($T \geq 200$ K), the increase of thermally induced electronic transitions across the narrow bandgap results in larger dark currents, overshadowing the detection of optically generated

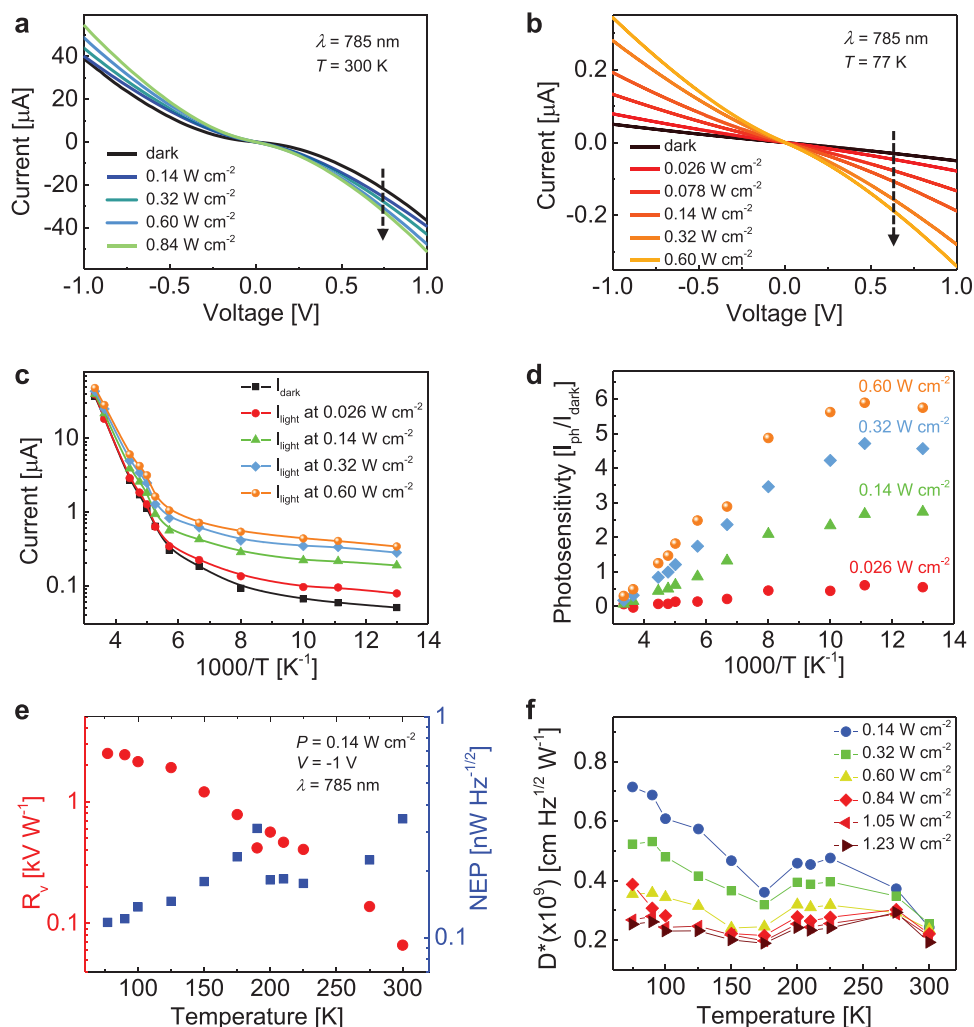


Figure 2. Device characterization under 785 nm illumination. a,b) I – V curves for different power densities of 785 nm wavelength at 300 and 77 K, respectively. c) Temperature dependence of current in dark (I_{dark}) and under illumination (I_{light}) for various power densities at a bias of -1 V. d) Photosensitivity ($I_{\text{ph}}/I_{\text{dark}}$) versus temperature at various laser power densities at an applied bias of -1 V. e) Temperature dependence of voltage responsivity and NEP at $P = 0.14 \text{ W cm}^{-2}$ and -1 V bias. f) Temperature dependence of detectivity at -1 V bias at various power densities.

charge carriers upon light illumination. This reverses at lower temperatures ($77\text{ K} \leq T < 200\text{ K}$) where photocurrent tends to remain constant and clearly dominates the dark current. In the low temperature range, the photodetector performance is, thus, governed mainly by optically generated charge carriers for the analyzed range of incident laser powers. To quantify these effects, photodetector photosensitivity ($I_{\text{ph}}/I_{\text{dark}}$)^[27,28] is plotted as a function of inverse temperature (Figure 2d). The photosensitivity is found to increase significantly with decreasing temperature; 6 at 77 K as opposed to 0.3 at 300 K ($P = 0.60\text{ W cm}^{-2}$, $\lambda = 785\text{ nm}$). While a notable change in the photosensitivity is observed at 77 K even for a low power density of 0.026 W cm^{-2} , at 300 K there is no measurable photocurrent until the incident power is increased tenfold, further affirming the improved performance at lower temperatures. In addition, photosensitivity also increases with laser power density, correlating to improved photocurrent generation. To reveal the device performance, we characterized other important figures of merit including responsivity, NEP, and D^* . Due to the linear and symmetric I - V characteristics, the MOF-photodetector operates in photoconductive mode. In a photoconductor, the absorption quantum efficiency (η_{abs}) can be defined as a function of absorption coefficient (α) and thickness of the active layer (t), $\eta_{\text{abs}} = (1 - r)(1 - \exp(-\alpha t))$, where r accounts for surface reflection losses.^[29,30] From the estimated reflection losses of $5\% \pm 1\%$ and $\alpha = 24\,900 \pm 3000\text{ cm}^{-1}$ (extracted from the Tauc plot in Figure 1c at $\lambda = 866\text{ nm}$), η_{abs} of $94\% \pm 1\%$ is obtained for the $1.7\text{ }\mu\text{m}$ thick MOF-device. Assuming that all absorbed photons contribute to the photocurrent, the quantum efficiency η is considered the same as the absorption quantum efficiency, that is, $\eta = \eta_{\text{abs}}$. Since the Fourier-transform infrared spectroscopy (FTIR) measurements reveal an invariant and high absorption over the UV-NIR spectral region (reported elsewhere, ref. [17]), the absorption coefficient estimated above can be applied to the whole analyzed spectral range. The responsivity ($R = I_{\text{ph}}/(P \times A)$; P is incident power density, A is exposed device area)^[31] is found to be 4 mA W^{-1} at 300 K ($\lambda = 785\text{ nm}$, $P = 0.14\text{ W cm}^{-2}$, $V = -1\text{ V}$), which is comparable to the values obtained for the first demonstrations of photodetectors based on black phosphorus (4.8 mA W^{-1})^[32] and graphene ($<6\text{ mA W}^{-1}$).^[33,34] However, in the present device configuration, responsivity is strongly dependent on device geometry and can vary significantly with the active area of the photodetector.^[35] In this respect, we further analyzed the voltage responsivity R_v , defined as the change in voltage drop per unit incident power across the detector, since R_v is independent of the device area.^[30] At low incident powers, it can be expressed as $R_v = (R \times V)/I_{\text{dark}}$, giving rise to $R_v = 2.5$ and 0.07 kV W^{-1} at 77 and 300 K, respectively. The temperature dependence of R_v is plotted in Figure 2e and shows a continuous increase with decreasing temperature. Another important parameter to evaluate the performance of the photodetector is NEP. It is defined as the detection limit of the photodetector and is a function of the detector's noise level, expressed as

$$\text{NEP} = \frac{\overline{I_n}^{-1/2}}{R} \quad (1)$$

where R is the responsivity and $\overline{I_n}^{-1/2}$ is the root mean square of the total noise current.^[36,37] The fundamental noise sources

in a photoconductor are Johnson noise (I_j), generation-recombination (G - R) noise (I_{gr}), and $1/f$ noise (I_f), the latter being dominant at low frequencies.^[29,30] From the photocurrent measurements, the Johnson noise is calculated as $[4kT\Delta f/R_d]^{1/2}$, where k is the Boltzmann constant, T is the absolute temperature, Δf is the bandwidth and R_d is the resistance of the device.^[29,30] For the MOF-device, the values of I_j are found to be $7.81 \times 10^{-13}\text{ A Hz}^{-1/2}$ at 300 K, which decreases to $1.44 \times 10^{-14}\text{ A Hz}^{-1/2}$ at 77 K ($P = 0.14\text{ W cm}^{-2}$, $\lambda = 785\text{ nm}$). The G - R noise, calculated as $[4qGI_{\text{dark}}\Delta f]^{1/2}$, where q is the electronic charge, and G is the photoconductive gain (calculated as $G = Rhc/\eta q\lambda$),^[30,38] is found to be ranging from 3.11×10^{-13} at 300 K to $2.60 \times 10^{-15}\text{ A Hz}^{-1/2}$ at 77 K. While the Johnson noise and the G - R noise estimations are straightforward, the $1/f$ noise is difficult to analyze analytically and is currently out of the scope of this work. Therefore, only Johnson noise and G - R noise are considered for the calculation of NEP. An NEP value as low as possible is desirable for an efficient and sensitive photodetector, which for $\text{Fe}_3(\text{THT})_2(\text{NH}_4)_3$ MOF-photodetectors is achieved by lowering the operating temperature (Figure 2e). Finally, we investigated the influence of temperature on the D^* , a measure of normalized signal-to-noise performance. D^* is derived by normalizing the inverse of NEP by detector area (A), $D^* = A^{1/2}/\text{NEP}$, for various laser power densities.^[37,39]

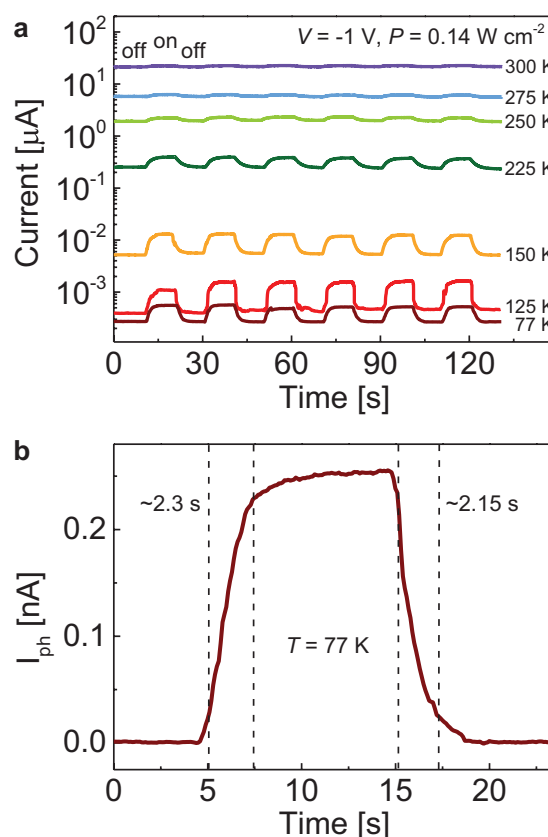


Figure 3. Photoswitching behavior under pulsed illumination of 785 nm laser. a) Temperature-dependent photoresponse as a function of time at $P = 0.14\text{ W cm}^{-2}$ and $V = -1\text{ V}$. The device shows long-term stable photoswitching capability. b) Time-resolved response zoomed, for 77 K, showing a response time of $\approx 2\text{ s}$.

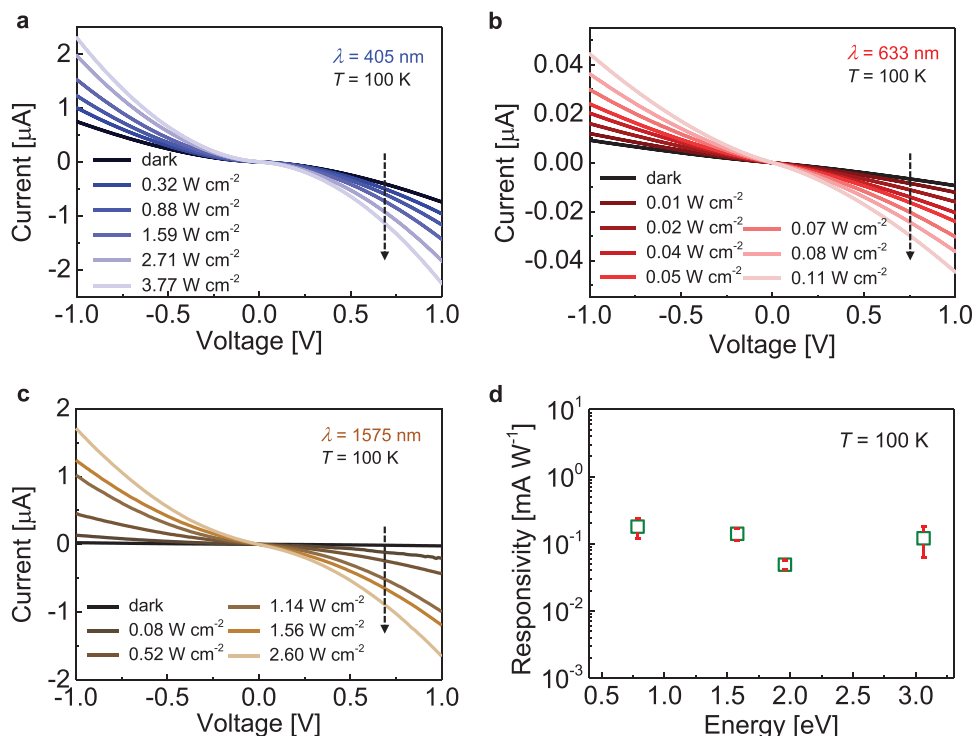


Figure 4. a–c) Photoresponse of the MOF detector at 100 K at 405 nm (a), 633 nm (b), and 1575 nm (c). d) Responsivity as a function of photon energy at a constant laser power density $P = 0.14 \text{ W cm}^{-2}$ and $T = 100 \text{ K}$.

Figure 2f shows an increase in D^* of the photodetector as the temperature decreases, with a peak D^* of $7 \times 10^8 \text{ cm Hz}^{1/2} \text{ W}^{-1}$ achieved at 77 K. It should be noted that the estimated NEP values (and hence, D^*) depend on the assumption that all absorbed photons generate free charge carriers. There is a possibility that a part of the absorption is “parasitic”, that is, some photons are lost without contributing to any photocurrent, leading to additional (typically, $1/f$) noise. Such a scenario would imply a higher gain, larger NEP, and smaller D^* values. Since this scenario is currently neglected, the estimations of NEP and D^* are valid only under the assumptions that the total noise comprises of only Johnson noise and G–R noise, and that the quantum efficiency equals the absorption efficiency. Therefore, our calculations provide a lower limit estimate of NEP and an upper limit of D^* values for the developed MOF-photodetectors.

The photoswitching performance of the MOF-photodetector is evaluated by testing the response of the MOF-device to light/dark cycles of illumination at 785 nm at various temperatures. Irrespective of temperature, a strong and reproducible switching behavior is revealed in Figure 3a, which demonstrates a stable operation of the MOF-device under pulsed irradiation. The response times for both rise and decay processes are extracted from the data as the time required by the photodetector to reach from 10% to 90% of the peak photocurrent after the illumination is turned on and vice versa after it is turned off, respectively.^[31,32] From Figure 3b, the rise and decay times at 77 K are found to be 2.3 and 2.15 s, respectively, an increase from $\approx 1.7 \text{ s}$ for both at 300 K. On testing multiple samples, response times in the range of 1–3 s are obtained. These response times are affected severely by the types and density of defects either intrinsic to the material

and/or arising during device fabrication processes.^[28,39,40] Previous reports have shown that by modulating these defects in a controlled manner, faster response times can be achieved.^[28,39–42] A brief discussion of potential defects present in our samples and ways to mitigate them is included in Supporting Information.

The spectral response of the MOF-photodetector at other wavelengths is tested by laser irradiations at wavelengths of 405, 633, and 1575 nm. The results obtained at these wavelengths are summarized in Figure 4a–c. An enhancement of the current at all wavelengths confirms the broadband photodetection operation in the UV-to-NIR range. The photocurrent (I_{ph}) increases with the laser power density (P) in accordance with the power law, $I_{\text{ph}} \propto P^\gamma$ with the exponent (γ) ranging 0.92 ± 0.09 for all analyzed wavelengths. Temperature-dependent photocurrent and photoswitching measurements performed at these wavelengths are shown in Figures S3–S5, Supporting Information. These results further confirm the improvement in the detector’s performance, once it is cooled to lower temperatures. While the response time lies in the range of 1–3 s, the detector demonstrates a stable and reproducible photoswitching behavior in the analyzed spectral range. The responsivity calculated for all impinging wavelengths at 100 K is plotted in Figure 4d. Since $\text{Fe}_3(\text{THT})_2(\text{NH}_4)_3$ MOF has high absorption in the UV–NIR region, no significant change in the quantum efficiency at these wavelengths is expected, which is consistent with the observed wavelength-independent responsivity. At these wavelengths, NEP and D^* are calculated by using the approach described before. The NEP values at 100 K ($P = 0.14 \text{ W cm}^{-2}$, $V = -1 \text{ V}$) are found to be $2.8 \text{ nW Hz}^{-1/2}$ (405 nm), $0.33 \text{ nW Hz}^{-1/2}$ (633 nm), and $0.07 \text{ nW Hz}^{-1/2}$ (1575 nm). The corresponding D^* values are estimated to be

$3 \times 10^7 \text{ cm Hz}^{1/2} \text{ W}^{-1}$ (405 nm), $3 \times 10^8 \text{ cm Hz}^{1/2} \text{ W}^{-1}$ (633 nm), and $2 \times 10^9 \text{ cm Hz}^{1/2} \text{ W}^{-1}$ (1575 nm).

In summary, this work reports a proof-of-concept photo-detector device based on semiconducting $\text{Fe}_3(\text{THT})_2(\text{NH}_4)_3$ 2D MOF films operating in a broad spectral range (400–1575 nm). A systematic study of the photoresponse dependence on temperature, wavelength, and incident laser power is carried out for the first time to fully address the performance of the MOF-device. Significant improvements in the performance of the device are achieved by cooling the detector to lower temperatures, due to the suppression of thermally activated charge carriers. While our findings show a promising future for MOF-based photodetection, opportunities for further improvements by optimizing the device configuration, fabrication of reliable contacts, and structural engineering of the material still exist. Owing to synthetic flexibility, large-area coverage, and cost-effective production of 2D conjugated MOFs, these materials are promising candidates for a plethora of optoelectronic applications.

Experimental Section

FTIR Measurements: FTIR was performed using a Bruker Vertex 80v spectrometer. The spectral range was from 0.20 to 1.44 eV. The infrared source was a Global. The thermal radiation emitted from the Global was focused on the sample with a spot of around $2 \times 2 \text{ mm}^2$. A nitrogen-cooled MCT was used as the detector.

Optoelectronic Properties Measurements: Low-temperature photocurrent measurements were performed in a cryogenic probe station (Lake Shore Model CPX-VF) equipped with a continuous-wave (cw)-laser diode at 405, 633, and 785 nm wavelengths (Toptica ultra compact diode laser, IBEAM-SMART-S). The laser was coupled with an optical fiber (FC/APC), which was connected to a vacuum feed through adapter inside the probe station to illuminate the samples. For all measurements, the fiber tip was kept orthogonal and at a fixed distance from the sample. The features of the laser were controlled by a software provided by Toptica. The IR measurements were performed under direct illumination of a 1575 nm wavelength InP laser diode (Thor Labs, L1575G1), controlled by an external power supply. All electrical measurements were carried out in vacuum ($<10^{-7}$ mbar) using a parameter analyzer (Agilent 4156C). The photoresponse was measured at regular temperature intervals while cooling down from 300 to 77 K.

Supporting Information

Supporting Information is available from the Wiley Online Library or from the author.

Acknowledgements

The authors thank S. Winnerl for subject matter discussion and J. Franke for drawing the schematics. E.C. acknowledges financial support from the Max Planck Society, the regional government of Comunidad de Madrid under projects 2017-T1/AMB-5207 & P2018/NMT-4511 and support from the “Severo Ochoa” Programme for Centres of Excellence in R&D (MINECO, Grant No. SEV-2016-0686). R.D. acknowledges the financial support from ERC Starting Grant (FC2DMOF, No. 852909), Coordination Networks: Building Blocks for Functional Systems (SPP 1928, COORNET), and MSCA-ITN-ETN (ULTIMATE, 813036). This work was supported by the Initiative and Networking Fund of the Helmholtz Association of German Research Centers through the International Helmholtz Research School for Nanoelectronic Networks, IHRS NANONET (VH-KO-606).

Conflict of Interest

The authors declare no conflict of interest.

Keywords

2D semiconductors, broadband photodetectors, low-temperature photodetection, metal–organic frameworks, photosensitivity

Received: October 28, 2019

Revised: December 14, 2019

Published online: January 23, 2020

- [1] H. Li, M. Eddaoudi, M. O’Keeffe, O. M. Yaghi, *Nature* **1999**, *402*, 276.
- [2] H. Deng, S. Grunder, K. E. Cordova, C. Valente, H. Furukawa, M. Hmadeh, F. Gándara, A. C. Whalley, Z. Liu, S. Asahina, H. Kazumori, M. O’Keeffe, O. Terasaki, J. F. Stoddart, O. M. Yaghi, *Science* **2012**, *336*, 1018.
- [3] O. K. Farha, I. Eryazici, N. C. Jeong, B. G. Hauser, C. E. Wilmer, A. A. Sarjeant, R. Q. Snurr, S. T. Nguyen, A. Ö. Yazaydin, J. T. Hupp, *J. Am. Chem. Soc.* **2012**, *134*, 15016.
- [4] O. K. Farha, A. Ö. Yazaydin, I. Eryazici, C. D. Malliakas, B. G. Hauser, M. G. Kanatzidis, S. T. Nguyen, R. Q. Snurr, J. T. Hupp, *Nat. Chem.* **2010**, *2*, 944.
- [5] Q. L. Zhu, Q. Xu, *Chem. Soc. Rev.* **2014**, *43*, 5468.
- [6] D. Farrusseng, *Metal-Organic Frameworks: Applications from Catalysis to Gas Storage*, John Wiley & Sons, Hoboken, NJ, USA **2011**.
- [7] M. Eddaoudi, J. Kim, N. Rosi, D. Vodak, J. Wachter, M. O’Keeffe, O. M. Yaghi, *Science* **2002**, *295*, 469.
- [8] Z. Chen, K. Adil, Ł. J. Weseliński, Y. Belmabkhout, M. Eddaoudi, *J. Mater. Chem. A* **2015**, *3*, 6276.
- [9] F. X. Llabrés i Xamena, A. Abad, A. Corma, H. Garcia, *J. Catal.* **2007**, *250*, 294.
- [10] J. Lee, O. K. Farha, J. Roberts, K. A. Scheidt, S. T. Nguyen, J. T. Hupp, *Chem. Soc. Rev.* **2009**, *38*, 1450.
- [11] P. Horcajada, C. Serre, M. Vallet-Regí, M. Sebban, F. Taulelle, G. Férey, *Angew. Chem., Int. Ed.* **2006**, *45*, 5974.
- [12] M. X. Wu, Y. W. Yang, *Adv. Mater.* **2017**, *29*, 1606134.
- [13] M. G. Campbell, D. Sheberla, S. F. Liu, T. M. Swager, M. Dincă, *Angew. Chem., Int. Ed.* **2015**, *54*, 4349.
- [14] M. G. Campbell, S. F. Liu, T. M. Swager, M. Dincă, *J. Am. Chem. Soc.* **2015**, *137*, 13780.
- [15] G. Wu, J. Huang, Y. Zang, J. He, G. Xu, *J. Am. Chem. Soc.* **2017**, *139*, 1360.
- [16] C. Yang, R. Dong, M. Wang, P. S. Petkov, Z. Zhang, M. Wang, P. Han, M. Ballabio, S. A. Bräuninger, Z. Liao, J. Zhang, F. Schwotzer, E. Zschech, H. H. Klaus, E. Cánovas, S. Kaskel, M. Bonn, S. Zhou, T. Heine, X. Feng, *Nat. Commun.* **2019**, *10*, 3260.
- [17] R. Dong, P. Han, H. Arora, M. Ballabio, M. Karakus, Z. Zhang, C. Shekhar, P. Adler, P. S. Petkov, A. Erbe, S. C. B. Mannsfeld, C. Felser, T. Heine, M. Bonn, X. Feng, E. Cánovas, *Nat. Mater.* **2018**, *17*, 1027.
- [18] R. Dong, Z. Zhang, D. C. Tranca, S. Zhou, M. Wang, P. Adler, Z. Liao, F. Liu, Y. Sun, W. Shi, Z. Zhang, E. Zschech, S. C. B. Mannsfeld, C. Felser, X. Feng, *Nat. Commun.* **2018**, *9*, 2637.
- [19] A. A. Talin, A. Centrone, A. C. Ford, M. E. Foster, V. Stavila, P. Haney, R. A. Kinney, V. Szalai, F. El Gabaly, H. P. Yoon, F. Léonard, M. D. Allendorf, *Science* **2014**, *343*, 66.
- [20] L. Sun, M. G. Campbell, M. Dincă, *Angew. Chem., Int. Ed.* **2016**, *55*, 3566.
- [21] D. Sheberla, L. Sun, M. A. Blood-Forsythe, S. Er, C. R. Wade, C. K. Brozek, A. Aspuru-Guzik, M. Dincă, *J. Am. Chem. Soc.* **2014**, *136*, 8859.

- [22] V. Stavila, A. A. Talin, M. D. Allendorf, *Chem. Soc. Rev.* **2014**, *43*, 5994.
- [23] I. Stassen, N. Burtch, A. Talin, P. Falcaro, M. Allendorf, R. Ameloot, *Chem. Soc. Rev.* **2017**, *46*, 3185.
- [24] Y. Cui, J. Yan, Z. Chen, J. Zhang, Y. Zou, Y. Sun, W. Xu, D. Zhu, *Adv. Sci.* **2019**, *6*, 1802235.
- [25] J. H. Dou, L. Sun, Y. Ge, W. Li, C. H. Hendon, J. Li, S. Gul, J. Yano, E. A. Stach, M. Dincă, *J. Am. Chem. Soc.* **2017**, *139*, 13608.
- [26] A. J. Clough, J. M. Skelton, C. A. Downes, A. A. de la Rosa, J. W. Yoo, A. Walsh, B. C. Melot, S. C. Marinescu, *J. Am. Chem. Soc.* **2017**, *139*, 10863.
- [27] A. F. Qasrawi, N. M. Gasanly, *Semicond. Sci. Technol.* **2005**, *20*, 446.
- [28] B. Cao, X. Shen, J. Shang, C. Cong, W. Yang, M. Eginligil, T. Yu, *APL Mater.* **2014**, *2*, 116101.
- [29] A. Rogalski, *Infrared Detectors*, Gordon and Breach Science Publishers, Amsterdam **2000**.
- [30] G. D. Dereniak, E. L. Boreman, *Infrared Detectors and Systems*, John Wiley & Sons, New York **1996**.
- [31] H. Arora, Y. Jung, T. Venanzi, K. Watanabe, T. Taniguchi, R. Hübner, H. Schneider, M. Helm, J. C. Hone, A. Erbe, *ACS Appl. Mater. Interfaces* **2019**, *11*, 43480.
- [32] M. Buscema, D. J. Groenendijk, S. I. Blanter, G. A. Steele, H. S. J. van der Zant, A. Castellanos-Gomez, *Nano Lett.* **2014**, *14*, 3347.
- [33] T. Mueller, F. Xia, P. Avouris, *Nat. Photonics* **2010**, *4*, 297.
- [34] F. Xia, T. Mueller, Y. M. Lin, A. Valdes-Garcia, P. Avouris, *Nat. Nanotechnol.* **2009**, *4*, 839.
- [35] R. Singh, V. Mittal, *Def. Sci. J.* **2003**, *53*, 281.
- [36] H. Arora, P. E. Malinowski, A. Chasin, D. Cheyng, S. Steudel, S. Schols, P. Heremans, *Appl. Phys. Lett.* **2015**, *106*, 143301.
- [37] X. Qiu, X. Yu, S. Yuan, Y. Gao, X. Liu, Y. Xu, D. Yang, *Adv. Opt. Mater.* **2018**, *6*, 1700638.
- [38] V. D. Shadrin, V. V. Mitin, V. A. Kochelap, K. K. Choi, *J. Appl. Phys.* **1995**, *77*, 1771.
- [39] B. Y. Zhang, T. Liu, B. Meng, X. Li, G. Liang, X. Hu, Q. J. Wang, *Nat. Commun.* **2013**, *4*, 1811.
- [40] O. Lopez-Sanchez, D. Lembke, M. Kayci, A. Radenovic, A. Kis, *Nat. Nanotechnol.* **2013**, *8*, 497.
- [41] R. H. Bube, *Photoelectric Properties of Semiconductors*, Cambridge University Press, Cambridge, UK **1992**.
- [42] A. Rose, *Concepts in Photoconductivity and Allied Problems*, Robert E. Krieger Publishing Company, Huntington, NY, USA **1978**.